This is a repository copy of *Neutral stability curves of compressible Görtler flow generated by low-frequency free-stream vortical disturbances*.

Neutral stability curves of compressible Görtler flow generated by low-frequency free-stream vortical disturbances

Samuele Viaro and Pierre Ricco†

Department of Mechanical Engineering, The University of Sheffield, Sheffield, S1 3JD, UK

Accepted for publication in Journal of Fluid Mechanics 2019

Pre-transitional compressible boundary layers perturbed by low-frequency free-stream vortical disturbances and flowing over plates with streamwise concave curvature are studied via matched asymptotic expansions and numerically. The Mach number, the Görtler number, and the frequency of the free-stream disturbance are varied to obtain the neutral stability curves, i.e. curves in the space of the parameters that distinguish spatially growing from spatially decaying perturbations. The receptivity approach is used to calculate the evolution of Klebanoff modes, highly-oblique Tollmien-Schlichting waves influenced by the concave curvature of the wall, and Görtler vortices. The Klebanoff modes always evolve from the leading edge, the Görtler vortices dominate when the influence of the curvature becomes significant, and the Tollmien-Schlichting waves may precede the Görtler vortices for moderate Görtler numbers. For relatively high frequencies the triple-deck formalism allows us to confirm the numerical result of the negligible influence of the curvature on the Tollmien-Schlichting waves when the Görtler number is an order-one quantity. Experimental data for compressible Görtler flows are mapped onto our neutral-curve graphs and earlier theoretical results are compared with our predictions.

1. Introduction

In this paper we study pre-transitional compressible boundary layers evolving over concave surfaces and exposed to free-stream vortical disturbances. We focus on the neutral stability curves, i.e. curves that distinguish the regions of growth and decay of the boundary-layer perturbations in the space of the Mach number and the scaled wall curvature, frequency, and wavenumbers.

Viaro & Ricco (2018) extended the receptivity theory of Wu et al. (2011) for incompressible Görtler flow engendered by free-stream vortical disturbances to resolve the open problem of the non-uniqueness of the neutral curve, first pointed out by Hall (1983) for stationary Görtler vortices. Wu et al. (2011)'s framework is based on the unsteady boundary-region equations, which are derived from the full Navier-Stokes equations in the limit of low frequency and large Reynolds number, coupled with rigorous initial and outer boundary conditions that synthesize the effects of the oncoming free-stream disturbances. Viaro & Ricco (2018) showed that the neutral curve is unique if the oncoming disturbances, and therefore the initial and free-stream boundary conditions, are specified. They considered a wide range of curvatures and wavenumbers, and used the receptivity approach to track the streamwise evolution of the perturbations from the leading edge. The study of Viaro & Ricco (2018) thus confirms that the eigenvalue framework of El-Hady & Verma (1983) for stationary Görtler vortices is invalid for

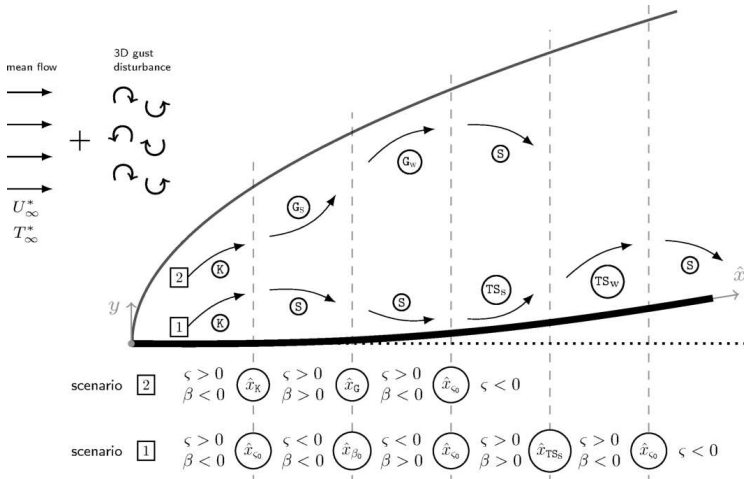† Email address for correspondence: p.ricco@sheffield.ac.uk

Figure 1: Schematic of the evolution of the perturbations for M=3, k_y=1, and $\mathcal{F}$=150 based on the parameters ς and β defined in (2.3) for the case of no G-vortices (G=0, scenario $\boxed{1}$) and the case of no TS$_{cc}$-waves (G>G$_E$, scenario $\boxed{2}$). The letter S indicates stable flow and the Görtler number G$_E$ is defined in figure 4.

the computation of the neutral curves and it is only applicable for large spanwise wavenumbers, as shown by Hall & Malik (1989).

We herein use the receptivity theory of Viaro & Ricco (2019) for compressible flows over streamwise-concave surfaces to analyze the effect of compressibility on the neutral curves computed by Viaro & Ricco (2018). We adopt the same notation, mathematical framework, and numerical approach of Viaro & Ricco (2019), so the reader is referred to that publication for further details. We investigate the effect of the Görtler number, the frequency, and the Mach number, and in particular the impact of the oblique Tollmien-Schlichting (TS) waves, studied by Ricco & Wu (2007) in the flat-plate case, on the neutral curves. We confirm our numerical results by using the triple-deck theory to prove that, at leading order, the curvature does not influence the TS-wave instability and we conclude by mapping experimental data on our neutral-curve graphs and by comparing our predictions with earlier theoretical results.

2. Mathematical framework

2.1. *Flow definition and scaling*

We consider a uniform compressible air flow of velocity U_∞^* and temperature T_∞^* past an adiabatic streamwise-concave plate with constant radius of curvature r^*. The flow domain is shown in figure 1 and we use the asterisk * to identify dimensional quantities. A kinematic and thermal boundary layer forms over the curved plate. Vortical disturbances are passively advected by the uniform free-stream flow and are modeled as three-dimensional gusts, which, sufficiently upstream and away from the plate, have the form

$$\mathbf{u} - \mathbf{i} = \epsilon \hat{\mathbf{u}}^\infty \, e^{i\left(\mathbf{k}\cdot\mathbf{x} - k_x R \hat{t}\right)} + \text{c.c.}, \qquad (2.1)$$

where ϵ is a small parameter, $\mathbf{x}=\{x, y, z\}$ denotes the streamwise, wall-normal, and spanwise directions, $\mathbf{k}=\{k_x, k_y, k_z\}$ defines the wavenumber vector, $\hat{\mathbf{u}}^\infty=\{\hat{u}^\infty, \hat{v}^\infty, \hat{w}^\infty\}$ is the amplitude of the free-stream disturbance, c.c. indicates the complex conjugate,

and $\mathbf{i}$ is the unit vector of the streamwise direction. The vectors $\mathbf{k}$ and $\hat{\mathbf{u}}^\infty$ satisfy the solenoidal condition $\mathbf{k}\cdot\hat{\mathbf{u}}^\infty=0$. Lengths are scaled by $\Lambda_z^*=\lambda_z^*/2\pi$, where λ_z^* is the spanwise wavelength of the gust, velocities are scaled by U_∞^*, and the pressure is scaled by $\rho_\infty^* U_\infty^{*2}$, where ρ_∞^* is the free-stream air density. The Reynolds number is $\mathtt{R}=U_\infty^*\Lambda_z^*/\nu_\infty^*\gg 1$, where ν_∞^* is the kinematic viscosity of air in the free stream, the Görtler number is $\mathtt{G}=\mathtt{R}^2\Lambda_z^*/r^*=\mathcal{O}(1)$, and the Mach number is $\mathtt{M}=U_\infty^*/a_\infty^*=\mathcal{O}(1)$, where $a_\infty^*=(\gamma\mathcal{R}^* T_\infty^*)^{1/2}$ is the speed of sound in the free stream, $\mathcal{R}^*=287.06$ J kg^{-1} K^{-1} is the ideal gas constant for air, and $\gamma=1.4$ is the ratio of specific heats. The scaled spanwise wavenumber is $k_z=1$ and the frequency parameter is $\mathcal{F}=k_x\mathtt{R}=2\pi\Lambda_z^{*2}U_\infty^*/(\lambda_x^*\nu_\infty^*)$. The coordinate x^* and time t^* are scaled as $\hat{x}=x^*/(\mathtt{R}\Lambda_z^*)$ and $\hat{t}=U_\infty^* t^*/(\mathtt{R}\Lambda_z^*)$ because low-frequency streamwise-elongated perturbations are dominant in the boundary layer.

The boundary-layer velocity, pressure, and temperature $\mathbf{q}(\mathbf{x},t)=\{u,v,w,p,\tau\}(\mathbf{x},t)$ are decomposed into their mean $\mathbf{Q}(\mathbf{x})$ and perturbation $\mathbf{q}'(\mathbf{x},t)$ as $\mathbf{q}=\mathbf{Q}+\epsilon\mathbf{q}'$. As in Viaro & Ricco (2019), the mean flow $\mathbf{Q}(\mathbf{x})$ is the compressible Blasius boundary layer without an externally-imposed pressure gradient. The Dorodnitsyn-Howarth transformation is used to scale the mean-flow equations in similarity form, for which the independent similarity variable is $\eta=\bar{Y}/(2\hat{x})^{1/2}$, where $\bar{Y}(\hat{x},y)=\int_0^y [T(\hat{x},\bar{y})]^{-1}\,\mathrm{d}\bar{y}$. The dynamic viscosity is modeled as $\mu(T)=T^\omega$, where $\omega=0.76$, and the constant Prandtl number is $\mathtt{Pr}=0.707$. The perturbations are defined as

$$\mathbf{q}' = ik_z\breve{w}\left\{\mathtt{R}\bar{u},\,(2\hat{x})^{1/2}\bar{v},\,\frac{1}{ik_z}\bar{w},\,\frac{1}{\mathtt{R}}\bar{p},\,\mathtt{R}\bar{\tau}\right\} e^{i\left(k_z z-\mathcal{F}\hat{t}\right)} + \text{c.c.}, \qquad (2.2)$$

where $\breve{w}\equiv\hat{w}^\infty+ik_z\hat{v}^\infty/(k_x^2+k_z^2)^{1/2}=\mathcal{O}(1)$ and $\bar{\mathbf{q}}(\hat{x},\eta)=\{\bar{u},\bar{v},\bar{w},\bar{p},\bar{\tau}\}(\hat{x},\eta)$. As explained by Leib et al. (1999) and Wu et al. (2011), the three-dimensional perturbations $\bar{\mathbf{q}}$ is dominant inside the boundary layer. In the limits of large Reynolds number $\mathtt{R}\gg 1$, small perturbations $\epsilon\ll\mathtt{R}^{-1}$, and low frequency $k_x\ll 1$, the linearized unsteady boundary-region (LUBR) equations for the perturbation flow are recovered by inserting the decomposed $\mathbf{q}(\mathbf{x},t)$ into the full compressible Navier-Stokes and continuity equations, using (2.2), and collecting $\mathcal{O}(\epsilon)$ terms. The LUBR equations are coupled with the initial and boundary conditions derived through asymptotic matching to synthesize the effect of the oncoming free-stream vortical disturbances on the boundary layer (Leib et al. 1999; Viaro & Ricco 2019). A second-order implicit finite-difference scheme is employed to solve the LUBR equations (Ricco & Wu 2007), which are parabolic along the streamwise direction. The four order-one parameters describing the flow are $\mathtt{M}$, $\mathtt{G}$, k_y, and $\mathcal{F}$, accounting for the effects of compressibility, curvature, ratio of free-stream spanwise and wall-normal wavelengths, and frequency, respectively.

2.2. *Neutral curve parameters*

Viaro & Ricco (2019) showed that, in low-frequency incompressible flows over concave surfaces and for realistic streamwise distances, $\mathtt{TS}$-waves do not appear and the perturbations evolve as Klebanoff modes, labelled $\mathtt{K}$-modes, or Görtler vortices, labelled $\mathtt{G}$-vortices. However, for finite Mach number and relatively high frequency, Ricco & Wu (2007) showed that oblique first-mode $\mathtt{TS}$-waves, studied by Smith (1989) through the triple-deck formalism, are triggered over a flat plate by a leading-edge receptivity mechanism analogous to the one first discovered by Goldstein (1983) for the incompressible case. Therefore, in the presence of curvature, a low-frequency compressible boundary layer may be unstable due to $\mathtt{K}$-modes, $\mathtt{TS}$-waves, or $\mathtt{G}$-vortices. Following the work of Viaro & Ricco (2018), the neutral curves and the different regions of instability can be mapped

by the parameters

$$\varsigma(\hat{x}) \equiv \frac{\mathrm{d}\mathrm{E}(\hat{x})}{\mathrm{d}\hat{x}} \quad \text{and} \quad \beta(\hat{x}) \equiv \frac{\mathrm{d}^2 |\bar{u}(\hat{x})|_{\max}}{\mathrm{d}\hat{x}^2}, \tag{2.3}$$

where $\mathrm{E}(\hat{x}) \equiv \int_0^\infty |\bar{u}(\hat{x}, \eta)|^2 \mathrm{d}\eta$ is the scaled perturbation energy divided by $(2\hat{x})^{1/2}$ (Hall 1990) and $|\bar{u}(\hat{x})|_{\max} \equiv \max_\eta |\bar{u}(\hat{x}, \eta)|$ is the maximum along η of the amplitude of the streamwise velocity perturbation, which is dominant over the other velocity components inside the boundary layer.

Figure 1 represents a sketch of the instabilities categorized according to (2.3) for the cases of zero Görtler number, where no G-vortices appear (scenario $\boxed{1}$), and of sufficiently large Görtler number, for which no TS-waves are detected (scenario $\boxed{2}$). The flow is unstable for $\varsigma > 0$ and stable for $\varsigma < 0$, with $\varsigma = 0$ defining the neutral points located at $\hat{x} = \hat{x}_{\varsigma_0}$. For growing perturbations, the parameter β is instrumental in discriminating between perturbations that display an algebraic-type growth ($\beta < 0$), like the K-modes, and perturbations that display an exponential-type growth ($\beta > 0$), like the TS-waves and the G-vortices. The condition $\beta < 0$ distinguishes the K-modes from the other two perturbations only if it is used during the initial stage of the evolution. This is because TS-waves and G-vortices may also display a negative-β growth due to viscous attenuation, following an initial positive-β growth. The choice of classifying the perturbations growing with negative β from the leading edge as K-modes is supported by the theoretical studies of Goldstein & Wundrow (1998) and Leib et al. (1999). In the proximity of the leading edge, the spanwise viscous diffusion is negligible and the flow is thus described by the boundary-layer equations: the initial growth is $|\bar{u}(\hat{x}, \eta)| = \eta F''\hat{x}/2$, where $F(\eta)$ is the Blasius function, and therefore $\beta = 0$. However, in the most common cases for which the boundary-layer thickness is comparable with the spanwise wavelength, the spanwise viscous effects attenuate the initial linear growth, which results in the algebraic negative-β K-mode dynamics. The notation $\mathrm{TS}_{\mathrm{cc}}$ is used to indicate TS-waves that are affected by the concave curvature of the wall, but not sufficiently for the inviscid pressure-centrifugal imbalance of the G-vortices to be fully operational. This terminology is appropriate in a range of moderate Görtler numbers, although TS-waves and G-vortices become indistinguishable from each other as the Görtler number increases. We indicate TS-waves without the subscript cc when we refer to instability waves for cases with G=0.

3. Results

3.1. *Effect of Mach number on the neutral curves*

We first study the effect of compressibility on the neutral curves in the steady Görtler case ($\mathcal{F} = 0$). Figure 2 (left) shows the stabilizing influence of the Mach number on the neutral stability curves, i.e. the stable region becomes larger as M increases. This effect is more intense at supersonic Mach numbers in agreement with the results of Viaro & Ricco (2019) and previous studies (El-Hady & Verma 1983; Hall & Malik 1989). Figure 2 (right) shows that the gap between the Görtler number corresponding to the local maximum, $\mathrm{G}_{\mathrm{C}_1}$, and the Görtler number corresponding to the local minimum, G_B, (both represented in Figure 2, left) grows as M increases, with $\mathrm{G}_{\mathrm{C}_1}$ influenced the most by compressibility. For $\mathrm{G} > \mathrm{G}_{\mathrm{C}_1}$ the perturbation shifts directly from Klebanoff modes to Görtler vortices, whereas for $\mathrm{G} < \mathrm{G}_\mathrm{B}$ no Görtler vortices are generated, even though the curvature is present.
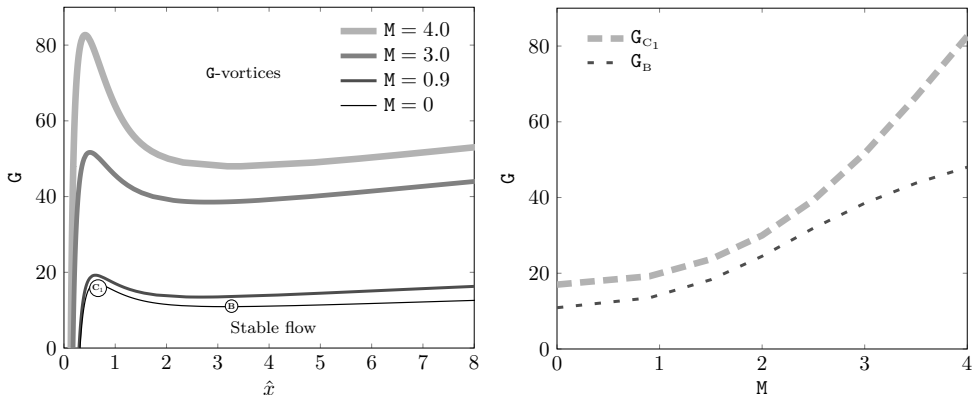
Figure 2: Left: Neutral stability curves, $\hat{x}=\hat{x}_{\varsigma_0}$, for different M values, $\mathcal{F}=0$, and $k_y=2$. Right: influence of M on the critical Görtler numbers $\mathtt{G_B}$ and $\mathtt{G_{C_1}}$, shown in the left graph.
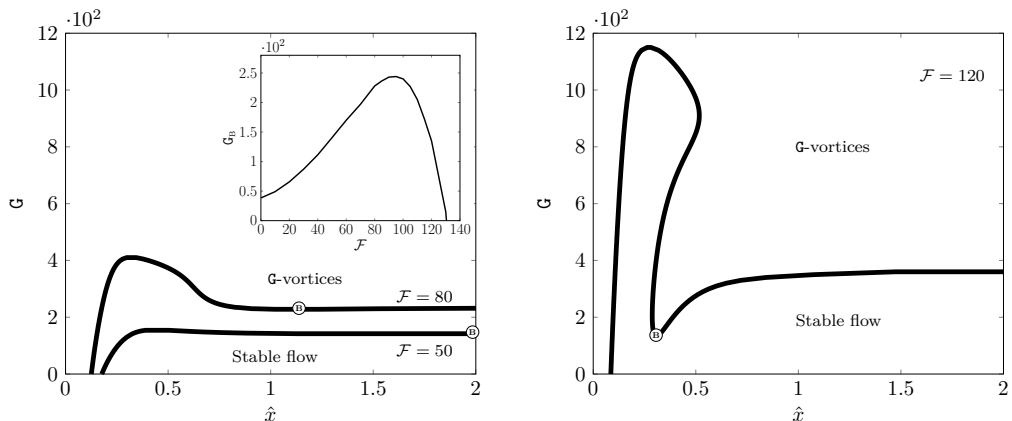

Figure 3: Evolution of the neutral stability curves $\hat{x}=\hat{x}_{\varsigma_0}$ as $\mathcal{F}$ increases for M=3 and $k_y=1$. Inset: Influence of $\mathcal{F}$ on $\mathtt{G_B}$.

3.2. *Effect of frequency on the neutral curves*

The change of the neutral curve in figure 2 (left) as the frequency increases is in figures 3 and 4 for M=3. The stable region expands as $\mathcal{F}$ grows. The inset of figure 3 (left) shows that $\mathtt{G_B}$ increases with $\mathcal{F}$ up to $\mathcal{F}=90$, but it rapidly drops at larger $\mathcal{F}$, as shown in figure 3 (right). It reaches zero when $\mathcal{F}=130.5$. For $\mathcal{F}<130.5$, no instability is found in the flat-plate case (G=0) other than the K-modes. For $\mathcal{F}>130.5$ two separate stable regions and a new critical $\mathtt{G_B}$ appear ($\mathtt{G_B}=437$ for $\mathcal{F}=150$). Figure 4 shows that at $\mathcal{F}=150$ the stable region $\mathtt{S_1}$ is confined by nearly vertical lines, which demonstrates that the effect of curvature on $\mathtt{S_1}$ is limited. As $\mathcal{F}$ increases, $\mathtt{G_{C_1}}$ increases rapidly and the vertical lines confining the stable region $\mathtt{S_1}$ become more parallel to the ordinate axis.

3.3. *Regions of instability*

We further analyze the case for $\mathcal{F}=150, \mathtt{M}=3$, and $k_y=1$, shown in figure 4. At these flow conditions the neutral-stability map reveals that the boundary layer can experience the three types of instability, i.e. the K-modes, the $\mathtt{TS_{cc}}$-waves, and the G-vortices. We identify the conditions for which these instabilities coexist using figures 5 and
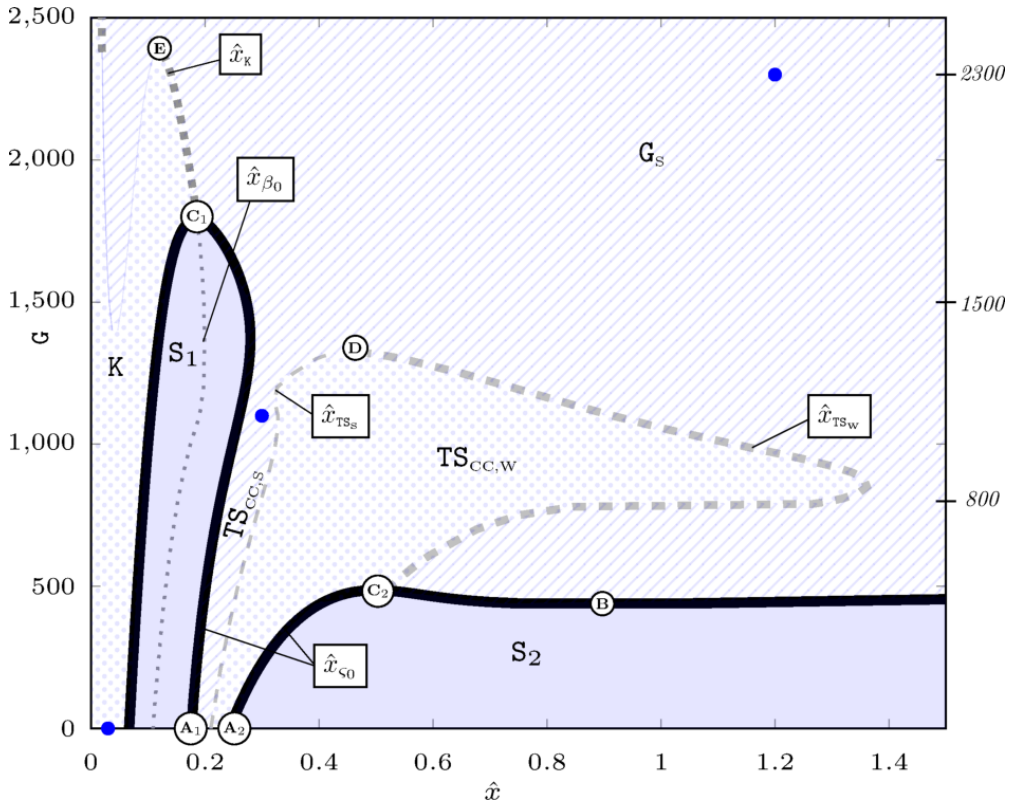
Figure 4: Neutral stability curve, $\hat{x}=\hat{x}_{\varsigma_0}$ (━━), and regions of instability for $\mathcal{F}=150$, $k_y=1$, and $\text{M}=3$. The blue full circles, located at $\{0.03, 0\}$, $\{0.3, 1000\}$, $\{1.2, 2300\}$, refer to the velocity profiles shown in figure 5.

6 to support the discussion. Figure 5 (left) shows the $\hat{x}$ evolution of the energy $\text{E}(\hat{x})$, scaled by the maximum value $\text{E}_{\max,\text{G}_0} \equiv \max_{\hat{x}} |\text{E}(\hat{x})|_{\text{G}=0}$, for five representative Görtler numbers. The energy maxima, M_1 and M_2, and the energy minimum m_1 identify the conditions for which $\varsigma=0$. Figure 5 (right) displays the wall-normal profiles of $|\bar{u}(\hat{x}, \eta)|/|\bar{u}(\hat{x})|_{\max}$ that are representative of the three types of perturbation. Figure 6 shows the $\hat{x}$ evolutions of $\varsigma(\hat{x})$, the growth rate of the perturbation (left), and of $\beta(\hat{x})$, the curvature of the maximum velocity with respect to $\hat{x}$ (right).

Since curvature effects are not at work near the leading edge (Wu et al. 2011) and $\hat{x}$ is not large enough for the TS-wave receptivity mechanism studied by Ricco & Wu (2007) to operate, only K-modes initially grow from the leading edge with $\beta<0$ at any G due to the continuous free-stream forcing. The K-modes either stabilize downstream of the first encountered neutral line at $\hat{x}=\hat{x}_{\varsigma_0}$ or, for $\text{G}>\text{G}_{\text{C}_1}=1792$, turn directly into G-vortices at $\hat{x}=\hat{x}_\text{K}$, indicated by the thick gray dotted line in figure 4 (scenario $\boxed{2}$ of figure 1). This zero-β line continues inside S_1 as G decreases (thin gray dotted line, $\hat{x}=\hat{x}_{\beta_0}$) and identifies the conditions for which the perturbation decay changes from strong to weak.

For the flat-plate case ($\text{G}=0$), the only growing perturbations are the K-modes and the TS-waves. The K-modes start growing from the leading edge and dissipate rapidly downstream of M_1 due to viscous effects (Leib et al. 1999), as shown in figure 5 (left). The combined influence of the frequency and the Mach number triggers the TS-waves at

point A_1, which display a second energy peak at M_2. For these flow conditions, the TS-waves are weaker than the K-modes and decay downstream of point A_2, shown in figure 4. This case is represented by scenario $\boxed{1}$ in figure 1. If the frequency or the Mach number increase, the oblique TS waves grow rapidly and the instability onset moves closer to the leading edge. Ricco & Wu (2007) used the triple-deck formalism to study these cases at relatively high frequencies.

As the curvature is introduced, the imbalance between pressure and centrifugal forces energizes both the K-modes and the TS_{cc}-waves, but for $G<G_B$ this is not sufficient to alter the zero-G pattern qualitatively, thus resulting in a boundary layer without G-vortices. In figure 4 the thin gray dashed line represents the zero-β streamwise location $\hat{x}=\hat{x}_{TS_s}$ where the TS_{cc}-waves shift from a strong growth ($TS_{cc,s}$, $\beta>0$) to a weak growth ($TS_{cc,w}$, $\beta<0$). The key observation here is that the first growth with $\beta>0$ downstream of S_1 has to be of the TS_{cc}-wave type because it evolves continuously from the flat plate scenario for which centrifugal effects are absent. The influence of G on the onset of the TS-waves is mild as the neutral lines are almost vertical. The negligible influence of the curvature on the TS_{cc}-waves for $G=\mathcal{O}(1)$ is supported by the triple-deck analysis in §3.4.

For $G>G_B$, the centrifugal effects intensify and the perturbation starts growing again with $\beta>0$ further downstream, i.e. the G-vortices appear. At $\hat{x}=\hat{x}_{TS_w}$ (thick gray dashed line), the strong-growth Görtler instability (G_s, $\beta>0$) ensues from the weakly growing TS_{cc}-waves (TS_{ccw}, $\beta<0$). Much further downstream at $\hat{x}=\hat{x}_G$ a weak G-vortex growth occurs (G_w, $\beta<0$) and ultimately a stable boundary layer is computed downstream of $\hat{x}=\hat{x}_{\varsigma_0}$ (not shown). In the range $G_{C_2}<G<G_D$ the region of weak TS_{cc}-wave instability widens downstream. As the curvature increases, the G-vortices move closer to the leading edge and the region of weak TS_{cc}-waves shortens.

For $G>G_D=1350$, the regime of weak TS_{cc}-wave growth disappears. The Görtler instability overcomes the weak negative-β TS_{cc}-wave growth and downstream of S_1 the perturbations always grow with $\beta>0$. Therefore, for $G>G_D$ the pressure-centrifugal imbalance caused by the curvature is sufficiently intense for the perturbation to grow as G-vortices immediately downstream of the stable region. The three types of boundary-layer instability thus occur only in the range $G_B<G<G_D$. In the top left corner of figure 4, we observe a very narrow streamwise region for $1400<G<G_E=2380$ where the K-modes show $\beta>0$. Downstream of this thin region, the K-modes recover the negative curvature and either start decaying in region S_1 for $1400<G<G_{C_1}$ or turn into G-vortices downstream of $\hat{x}=\hat{x}_K$ for $G>G_{C_1}$. For $G>G_E$, the K-modes show negative β at any $\hat{x}$ locations upstream of the Görtler growth.

3.4. *Asymptotic analysis at relatively high frequency*

We investigate the effect of curvature for $G=\mathcal{O}(1)$ on the highly oblique TS-waves generated by the receptivity mechanism first studied by Ricco & Wu (2007). We are motivated by the numerical result, shown in figure 4, of the negligible influence of curvature on the TS-wave growth and on the stable region S_1 for moderate G values.

The Görtler terms, found in the y-momentum equation (2.11) of Viaro & Ricco (2019) and scaled here in the ($\bar{x}=k_x x, \eta$) coordinate system for consistency with the receptivity analysis by Ricco & Wu (2007), are

$$\frac{G}{(2\bar{x})^{1/2}}\left[2F'\bar{u}(\bar{x},\eta)-\frac{F'^2}{T}\bar{\tau}(\bar{x},\eta)\right]\frac{\kappa}{k_z}, \tag{3.1}$$

where $\kappa=k_z\mathcal{F}^{-1/2}$ and $T(\eta)$ is the mean-flow temperature. Ricco & Wu (2007) demonstrated that the highly oblique TS-waves originate from decaying Lam-Rott eigensolu-
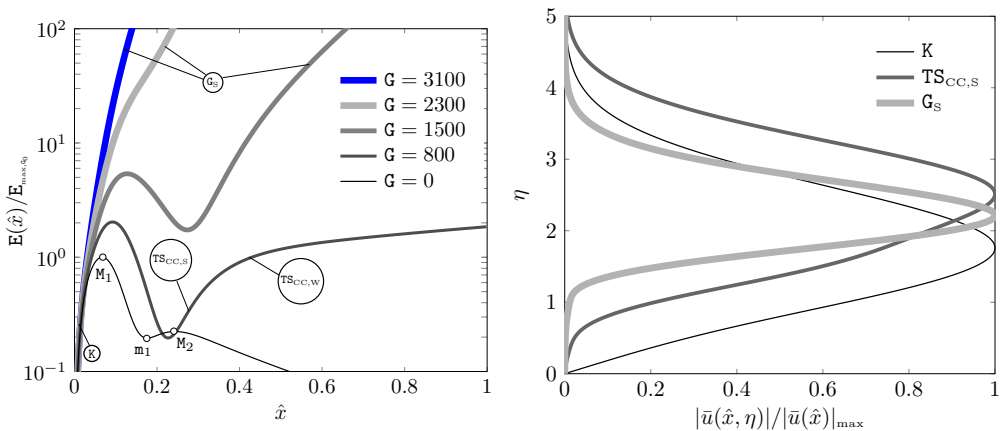
Figure 5: Evolution of $\mathrm{E}(\hat{x})/\mathrm{E}_{\max,\mathrm{G}_0}$ (left) and wall-normal profiles of $|\bar{u}(\hat{x},\eta)|/|\bar{u}(\hat{x})|_{\max}$ for the perturbations corresponding to the blue circles in figure 4 for $\mathcal{F}$=150, k_y=1, and M=3.
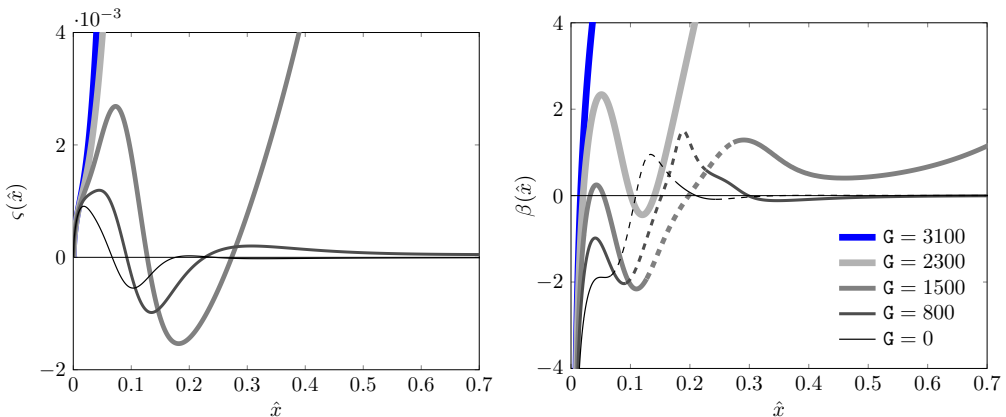

Figure 6: Evolution of $\varsigma(\hat{x})$ (left) and $\beta(\hat{x})$ (right), defined in (2.3), for $\mathcal{F}$=150, k_y=1, and M=3. In the right graph, the lines are solid when $\varsigma > 0$.

tions. Extending Ricco & Wu (2007)'s triple-deck analysis to flows over concave surfaces with $\kappa \ll 1$ and G=$\mathcal{O}(1)$, in the lower deck (subscript L) the Görtler terms (3.1) become

$$\frac{\mathrm{G}}{(2\bar{x})^{1/2}} \left[2F''(0)\eta_{\mathrm{L}}\bar{u}_{\mathrm{L}} - \frac{F''(0)^2}{T(0)}\eta_{\mathrm{L}}^2\bar{\tau}_{\mathrm{L}}\kappa \right] \frac{\kappa^2}{k_z} \ll \frac{\partial \bar{p}_{\mathrm{L}}}{\partial \eta_{\mathrm{L}}} = \mathcal{O}(1), \tag{3.2}$$

in the main deck (subscript M) they become

$$\frac{\mathrm{G}}{(2\bar{x})^{1/2}} \left(2F'\bar{u}_{\mathrm{M}} - \frac{F'^2}{T}\bar{\tau}_{\mathrm{M}} \right) \frac{\kappa^{3/2}}{k_z} \ll \frac{\partial \bar{p}_{\mathrm{M}}}{\partial \eta} = \mathcal{O}(1), \tag{3.3}$$

and in the upper deck (subscript U) they are

$$\frac{2\mathrm{G}\bar{u}_{\mathrm{U}}}{(2\bar{x})^{1/2}} \frac{\kappa^2}{k_z} \ll \frac{\partial \bar{p}_{\mathrm{U}}}{\partial \eta_{\mathrm{U}}} = \mathcal{O}(1), \tag{3.4}$$

where the pressure terms in (3.2), (3.3), and (3.4) are of the same order of the other terms
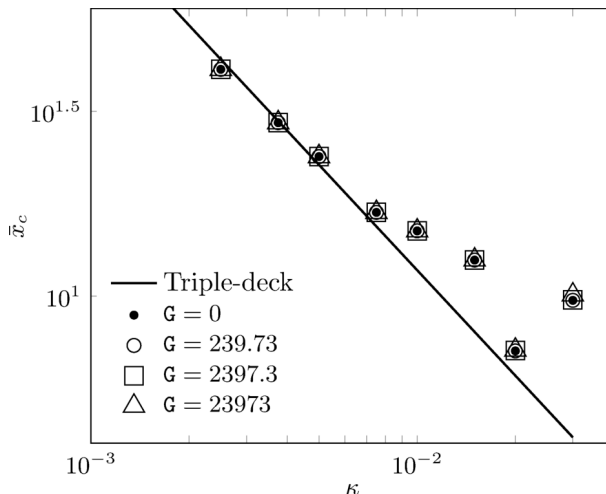
Figure 7: Influence of the Görtler number on the streamwise location $\bar{x}_c$ as a function κ for the triple-deck solution (continuous line) and the LUBR solution (symbols) for M=3 and k_y=1.

in the triple-deck y-momentum equations of Ricco & Wu (2007). The curvature terms are thus negligible at first order and the flat-plate dispersion relation for the streamwise wavenumber $\alpha_1(\bar{x})$ is recovered (Ricco & Wu 2007),

$$\int_{\eta_0}^{\infty} \mathtt{Ai}(\breve{\eta}) \mathrm{d}\breve{\eta} - (i\alpha_1)^{-1/3} \left[\frac{F''(0)}{(2x_1)^{1/2}} \right]^{5/3} \left[\frac{\mu(0)}{T(0)^7} \right]^{1/3} \mathtt{Ai}'(\eta_0) = 0, \qquad (3.5)$$

where $\mathtt{Ai}(\eta)$ is the Airy function, $x_1=\kappa\bar{x}=\mathcal{O}(1)$ is the scaled streamwise coordinate, and $\eta_0=-[2iF''(0)\alpha_1 x_1 T(0)/\mu(0)]^{1/3}/[\alpha_1 F''(0)]$. Numerical integration of (3.5) gives the local growth rate, $\mathtt{Im}(\alpha_1)$. Figure 7 graphically shows the critical streamwise location $\bar{x}_c$ where the $\mathtt{TS_{cc}}$-waves start to grow as a function of κ for different G values. Excellent agreement is found between the LUBR computation and the triple-deck theoretical solution, i.e. $\bar{x}_c$=Cκ^{-1}. This comparison allows us to compute the proportionality constant, C=3.32. The effect of the curvature only appears for $\kappa \geqslant 0.02$ and G$\geqslant$23973, which is consistent with the analytical results valid for $\kappa \ll 1$ and G=$\mathcal{O}(1)$. These findings give full support to the lines $\hat{x}_{\varsigma_0}$ confining the stable region $\mathtt{S_1}$ being nearly vertical for moderate G values, as shown in figure 4. As the frequency increases, these lines become even more parallel to the ordinate axis and extend to higher G values, which confirms that $\mathtt{TS}$-waves are not affected by the curvature when the frequency is sufficiently high. This also strengthens the argument that the perturbations downstream of the stable region $\mathtt{S_1}$ can be classified as $\mathtt{TS}$-waves for moderate G.

3.5. *Comparison with experimental data and previous theoretical results*

In figure 8, the neutral curves computed by the LUBR equations for $\mathcal{F}$=0 and k_y=1 are compared with neutral curves by other authors (dashed lines) for M=0 (left) and for M=3 (right). The figure also shows the positions $\hat{x}=\hat{x}_{\mathtt{K}}$ where the K-modes shift to G-vortices (dotted lines) and the streamwise locations and Görtler numbers of experimental data.

For M=0, figure 8 (left) shows that the theoretical neutral curve computed by the EV framework of El-Hady & Verma (1983) fails to capture the unstable region near the leading edge where the K-modes grow downstream. This is expected as the dynamics of
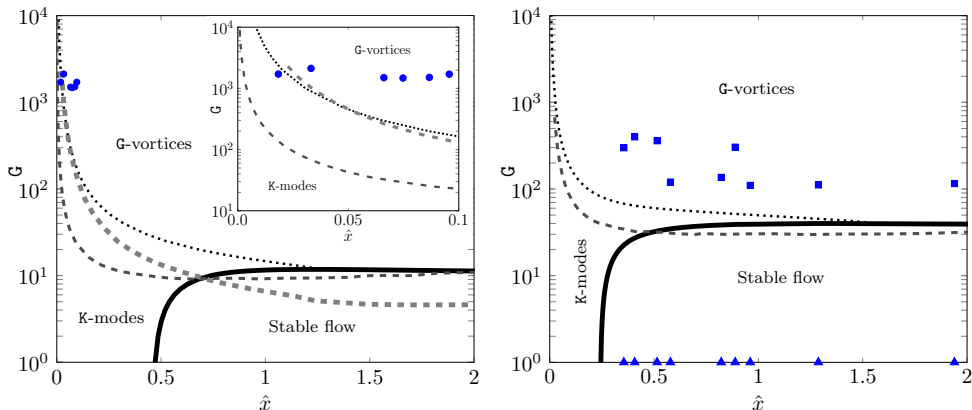
Figure 8: Comparison of the LUBR neutral curve (━━) at $\mathcal{F}=0$, $k_y=1$ with El-Hady & Verma (1983)'s neutral curves (━ ━ ━) and with Hall (1990)'s neutral curve (▪ ▪ ▪) for M=0 (left) and M=3 (right). Experimental data by Tani (1962) (●) and Ciolkosz & Spina (2006) (▪, ▲), and locations where the K-modes become G-vortices ($\hat{x}=\hat{x}_{\text{K}}$, ⋯⋯).

K-modes can only be computed through the inhomogeneous receptivity formalism of Leib et al. (1999) and Wu et al. (2011). The receptivity framework by Hall (1990) includes the effect of the oncoming disturbed flow and is therefore an improvement of Hall (1983)'s approach, where the initial conditions for the parabolic equations modelled vortices that were already inside the boundary layer without accounting for their generation caused by the free-stream disturbances. Hall (1990)'s neutral curve shows good agreement with our $\hat{x}_{\text{K}}$-line, downstream of which the G-vortices evolve from the K-modes. Nevertheless, Hall (1990)'s curve is unable to predict the K-mode growth. Tani (1962)'s experimental point of instability at the shortest distance from the leading edge is classified as stable by El-Hady & Verma (1983) and Hall (1990), whereas our computations predict this point as representative of growing K-modes. All the other points by Tani (1962) fall inside the unstable region and are thus identified as G-vortices. We compare Tani (1962)'s data with the neutral curve for $\mathcal{F}=0$ because, although Tani (1962) did not report the dominant frequency of their free-stream disturbance, Wu et al. (2011) showed excellent agreement between these data and their numerical results for steady conditions. The wind-tunnel incompressible data by Boiko et al. (2010) have been shown by Viaro & Ricco (2018) to fall within the region of Görtler instability.

As in the incompressible case, El-Hady & Verma (1983)'s neutral curve for M=3 in figure 8 (right) does not predict the algebraic growth from the leading edge, although the agreement with the LUBR solution improves as $\hat{x}$ increases. The experimental data by Ciolkosz & Spina (2006) at supersonic conditions, corresponding to perturbations with a spanwise wavelength equal to 0.2 mm, fall in the unstable region and are thus classified as G-vortices. Ciolkosz & Spina (2006) also measured the perturbations at the same locations and flow conditions over a flat plate and no growing perturbations were detected. This is also in agreement with our computations as these experimental points all lie in the stable zero-G region downstream of the K-mode growth.

hospitality of the Institute and in particular Dr Marvin E. Goldstein and Dr Stewart Leib for hosting SV. We are indebted to Dr Goldstein for the invaluable discussions about this research work.

REFERENCES

BOIKO, A.V., IVANOV, A.V., KACHANOV, Y.S. & MISCHENKO, D.A. 2010 Steady and unsteady Görtler boundary-layer instability on concave wall. *Europ. J. Mech. B/Fluids* **29** (2), 61–83.

CIOLKOSZ, L.D. & SPINA, E.F. 2006 An experimental study of Görtler vortices in compressible flow. *AIAA Paper* (4512), 1–21.

EL-HADY, N.M. & VERMA, A.K. 1983 Growth of Görtler vortices in compressible boundary layers along curved surfaces. *J. Eng. Applied Sc.* **2** (3), 213–238.

GOLDSTEIN, M.E. 1983 The evolution of Tollmien-Schlichting waves near a leading edge. *J. Fluid Mech.* **127**, 59–81.

GOLDSTEIN, M.E. & WUNDROW, D.W. 1998 On the environmental realizability of algebraically growing disturbances and their relation to Klebanoff modes. *Theor. Comp. Fluid Dyn.* **10**, 171–186.

HALL, P. 1983 The linear development of Görtler vortices in growing boundary layers. *J. Fluid Mech.* **130**, 41–58.

HALL, P. 1990 Görtler vortices in growing boundary layers: the leading edge receptivity problem, linear growth and the nonlinear breakdown stage. *Mathematika* **37** (74), 151–189.

HALL, P. & MALIK, M. 1989 The growth of Görtler vortices in compressible boundary layers. *J. Eng. Math.* **23** (3), 239–251.

LEIB, S.J., WUNDROW, D.W. & GOLDSTEIN, M.E. 1999 Effect of free-stream turbulence and other vortical disturbances on a laminar boundary layer. *J. Fluid Mech.* **380**, 169–203.

RICCO, P. & WU, X. 2007 Response of a compressible laminar boundary layer to free-stream vortical disturbances. *J. Fluid Mech.* **587**, 97–138.

SMITH, F.T. 1989 On the first-mode instability in subsonic, supersonic or hypersonic boundary layers. *J. Fluid Mech.* **198**, 127–153.

TANI, I. 1962 Production of longitudinal vortices in the boundary layer along a concave wall. *J. Geophys. Res.* **67** (8), 3075–3080.

VIARO, S. & RICCO, P. 2018 Neutral stability curves of low-frequency Görtler flow generated by free-stream vortical disturbances. *J. Fluid Mech.* **845** (R1).

VIARO, S. & RICCO, P. 2019 Compressible unsteady Görtler vortices subject to free-stream vortical disturbances. *J. Fluid Mech.* **867**, 250–299.

WU, X., ZHAO, D. & LUO, J. 2011 Excitation of steady and unsteady Görtler vortices by free-stream vortical disturbances. *J. Fluid Mech.* **682**, 66–100.